Flow and Drop Transport Along Liquid-Infused Surfaces

Pre-print: *Annual Reviews [1]of Fluid Mechanics* **54** (2022)

Flow and drop transport along liquid-infused surfaces

Steffen Hardt[1] and Glen McHale[2]

[1]Fachgebiet Nano- und Mikrofluidik, Fachbereich Maschinenbau, Technische Universität, Darmstadt, Darmstadt, Germany; email: hardt@nmf.tu-darmstadt.de

[2]Institute for Multiscale Thermofluids, School of Engineering, University of Edinburgh, Edinburgh, United Kingdom; email: glen.mchale@ed.ac.uk

1. Introduction

Biomimetic surfaces imitate the intriguing functionalities of surfaces found in nature. Superhydrophobic surfaces (SHS) form an important class of biomimetic surfaces, inspired, among others, by the surface morphology of the leaves of the Lotus plant (*Nelumbo nucifera*). Lotus leaves show water-repellent properties and suppress the adhesion of particles (Barthlott & Neinhuis 1997), properties that are desirable in many technological applications. Apart from such effects found in nature, superhydrophobic surfaces offer additional functionalities that are of interest in certain application areas. For example, superhydrophobic surfaces reduce drag in liquid flows (Rothstein 2010) and increase the efficiency of condensation processes (Boreyko & Chen 2009). However, their broadband application is hampered by their lack of robustness. For example, when the pressure in the liquid flow exceeds a certain threshold value, a wetting transition is triggered in which a superhydrophobic surface loses many of its favorable properties (Bormashenko 2010, Quéré 2008, Lafuma & Quéré 2003).

Liquid-infused surfaces (LIS) form another class of biomimetic surfaces. Also these surfaces are inspired by plants, specifically pitcher plants of the genus *Nepenthes*. These carnivorous plants have a pitcher in which they trap insects. Insects glide down into the pitcher because they "aquaplane" on a LIS (Bohn & Federle 2004). More than 15 years ago it was recognized that infusing a micro- or nanostructured solid surface with a low-surface

[1] This pre-print does not included subsequent changes agreed through the peer reviewer and editorial procedures

tension liquid may result in a slippery composite solid-liquid surface (Quéré 2005). The infused liquid, acting as a lubricant, is immiscible with the liquids contacting the surface. In 2011 artificial LIS with ultra-slippery features similar to those of the pitcher plant were established for the first time (Wong et al. 2011; see also Lafuma & Quéré 2011).

Especially the self-healing properties of LIS (Wong et al. 2011) spurred the hope that these surfaces might prove more robust than superhydrophobic surfaces in application scenarios. Here, "self-healing" refers to the fact that local perturbations or defects in the surface structure are repaired or compensated by capillary suction, i.e. the lubricant automatically fills voids or dry spots on the surface. By contrast, on a superhydrophobic surface the transition from the initial Cassie to the Wenzel state is very difficult to revert (Bormashenko 2010, Quéré 2008, Lafuma & Quéré 2003). A number of promising applications of LIS have already been demonstrated. For example, LIS have great potential to suppress ice formation (Kreder et al. 2016, Latthe et al. 2019) and fouling of surfaces (Epstein et al. 2012, Xiao et al. 2013), to provide stimuli-responsive functions (Lou et al. 2020), as well as for medical applications (Howell et al. 2018). Generally, the research area of LIS has expanded dramatically over the past few years. This includes methods for fabricating LIS with different morphologies, where the large selection of infusing liquids, surface topographies and surface chemistries offers a vast design space. In that context the reader is referred to recently published review articles (Solomon et al. 2017, Huang & Guo 2019, Villegas et al. 2019, Chen et al. 2020, Peppou-Chapman et al. 2020).

This review article focusses on the fluid mechanics on LIS, that is, the interaction of surfaces with a flow field and the behavior of drops on such surfaces. Such aspects of fluid mechanics form the foundations of a number of applications of LIS, addressing, for example, drag reduction or enhancement of water vapor condensation (Anand et al. 2012).

The article is structured as follows. Section 2 gives a brief account of the morphology of LIS, i.e. their composition and structural features. This section introduces some of the

fundamental concepts needed in subsequent sections. Section 3 addresses the interaction of LIS with a flow field, that is, single-phase flow. The focus is on the drag forces exerted by LIS and on the structure formation due to the flow that induces a re-distribution of lubricant. Section 4 deals with drops on LIS, specifically with static wetting and drop motion. Special attention is drawn to the question how far conventional concepts of wetting can be translated to wetting on LIS and to the origin of the frictional force experienced by drops translating along LIS.

2. Morphology of liquid-infused surfaces

Just like superhydrophobic surfaces, the design of LIS is inspired by nature. A significant inspiration are pitcher plants of the genus *Nepenthes*. These carnivorous plants have a pitcher in which they trap insects (Bohn & Federle 2004). Insects on the upper rim of the pitcher, the so-called peristome, glide down along the slippery surface and fall into the pitcher where they are digested by enzymes.

The reason why the peristome surface is so slippery lies in sophisticated microstructures and a design principle that challenge the most advanced concepts from micro- and nanotechnology (Chen et al. 2016). The peristome surface becomes slippery via infusion with an aqueous liquid, for example with nectar secreted by the plant or with rain water. Insects glide down because they "aquaplane" on this liquid-infused surface (Bohn & Federle 2004). The infusion of liquid into such surface structures is unidirectional and very fast (Chen et al. 2016).

Only some 10 years ago, scientists designed artificial LIS capable of reproducing the slippery surface performance of the peristome of the pitcher plant. In (Lafuma & Quere 2011), microstructured surfaces were reported where the trapped fluid was oil rather than air, representing a new class of materials, which are hemi-liquid and hemi-solid. Two qualitatively different wetting states were observed: one where the drops "float" on the mixed

substrate, which leads to low contact-angle hysteresis, and one where the drops "sink" and can pin on the solid defects, which significantly increases the contact-angle hysteresis. Independently, in (Wong et al. 2011) both periodic and random oil-infused textures were studied, where the focus was on the slippery state where a drop is separated from the solid by a continuous thin film of oil. Corresponding surfaces were termed "slippery liquid-infused porous surfaces" (SLIPS). Specifically, it was shown that such LIS, apart from aqueous drops, easily shed oil drops and that defects in the surface are self-healed by capillary suction. After these first demonstrations of artificial LIS, extensive research efforts were devoted to studying the properties of LIS and formulation of new surface designs.

The wetting morphologies of LIS can be inferred by considering the sum of the total interfacial energies between the solid (S), the infusing liquid (L) and the surrounding gas (G). For brevity, in the following the infusing liquid will be termed "lubricant" and the second liquid wetting the LIS "water". For concreteness, we imagine a surface topography consisting of structures with vertical walls and flat tops. An example would be a square array of posts of square cross section (width a) and height h, with an edge-to-edge spacing between neighboring posts of b. To decide whether or not the lubricant infuses the surface texture, we need to compare the interfacial energy of the infused state to that of a dry surface (Smith et al. 2013). The wetting morphology will also be influenced by the presence of water, for example in form of a drop. In the regions not covered by water, apart from a dry surface (configuration A), there are two other morphologies with lubricant infusing the textures, as shown in Figure 1. In the first version, the tops of the elevations remain dry (configuration B), in the second version they are covered with lubricant (configuration C). Turning our attention first to the scenario where only lubricant is present, the comparison between the interfacial energies of the different morphologies can be formulated in terms of the microscopic contact angle $\theta_{\mathrm{LS(G)}}$ between the lubricant, the solid surface and the surrounding gas. The wetting morphologies are governed by a critical contact angle $\cos\theta_{\mathrm{c}} = (1-\phi)/(r-\phi)$ which determines whether

imbibition occurs (Bico et al., 2001). In this expression, *r* is the ratio of the total surface area of the dry surface and the projected surface area, and ϕ is the area fraction of the flat tops. For the example of a square array of posts we obtain $r = 1 + 4ah/(a+b)^2$ and $\phi = a^2/(a+b)^2$. Expressed by the critical contact angle, the minimization of the total interfacial energy yields the following wetting morphologies (Smith et al. 2013): configuration A if $\theta_{\mathrm{LS(G)}} > \theta_{\mathrm{c}}$, configuration B if $0 < \theta_{\mathrm{LS(G)}} < \theta_{\mathrm{c}}$, configuration C if $\theta_{\mathrm{LS(G)}} = 0$.

The inclusion of a second liquid (water) complicates the picture. Depending on the specific values of the interfacial energy between solid and water, lubricant and water, as well as water and gas, the presence of water can change the wetting morphology of the lubricant-infused surface. It is possible that water displaces the lubricant from the surface texture, or displaces the lubricant film covering the tops of the elevations. Figure 1 shows a map of the possible wetting morphologies for a water drop sitting on a LIS (Smith et al. 2013). Apart from the value of $\theta_{\mathrm{LS(G)}}$, the configurations depend on the microscopic contact angle of the lubricant on the solid surrounded by water, $\theta_{\mathrm{LS(W)}}$. The map is spanned by two spreading coefficients $S_{\mathrm{LS(G)}}$ and $S_{\mathrm{LS(W)}}$, where the spreading coefficient is defined as $S_{ij(k)} = \gamma_{jk} - \gamma_{ij} - \gamma_{ik}$, γ denotes interfacial tension, and the subscripts *i*, *j*, *k* refer to different materials.

Many of the favorable properties of LIS are connected to the existence of a thin lubricant film separating the water phase from the solid, which means that usually the liquids are chosen such that $\theta_{\mathrm{LS(W)}} = 0$, or, equivalently $S_{\mathrm{LS(W)}} > 0$. In (Daniel et al. 2017) it was pointed out that this condition alone does not guarantee a stable lubricant film under a static drop. The reason is that for films as thin as the range of forces between the molecules in a fluid, the energetics of a configuration of different fluids can no longer be modeled solely based on interfacial tensions. In that case, for van-der-Waals interactions the disjoining

pressure $\Pi(h) = A/\left(6\pi h^3\right)$ needs to be considered, where h is the lubricant film thickness and A the Hamaker constant (Daniel et al. 2017). To obtain a stable lubricant film between the water phase and the solid, apart from $S_{\mathrm{LS(W)}} > 0$ a positive Hamaker constant is required. In a dynamic situation, for example when a drop moves along a LIS, the lubricant film underneath the water phase is no longer governed by a static force balance but by hydrodynamic effects, which will be discussed in Section 4.

The key to many applications of LIS involving drops is to construct surfaces that minimize pinning. To minimize pinning, micron-scale LIS textures can have an additional, typically nano-, length scale of roughness which retains lubricant and ensures that drops never directly contact the solid tops of the texture. This includes nano-grass on microposts (Figure 2a,b) (Anand et al., 2012) and superhydrophobic nano-particles on micro-scale textures (Guan et al., 2017; Keiser et al., 2017). These all follow the principle of hierarchical surfaces (Kim et al., 2013; Smith et al., 2013) and provide lubricant coatings following the underlying micro-scale texture shape. Such ideas have been implemented to create doubly re-entrant micro-pillars with lubricant-infused tops (Figure 2c,d) (Dong et al., 2018). Corresponding surfaces can support drops in an (ultra-slippery) Cassie state or a slippery Wenzel state (Figure 2e,f) (Dai et al. 2015). This idea of a conformal lubricant layer following the topography of an underlying solid structure can be re-conceptualized as shaped liquid surface (Launay et al., 2020). The other extreme are flat surfaces without any texture impregnated with a thin liquid film. In (Eifert et al., 2014) it was shown that when using a lubricant with a positive spreading coefficient, such surfaces can display properties very similar to textured LIS.

Designing LIS with sophisticated morphologies and extended functionalities is a current research trend. For example, recently textured surfaces exposing patterns of two different ILs were reported (Paulssen et al. 2018). On such surfaces, drops can be guided

along defined tracks or can be sorted according to size (Paulssen et al. 2019). Furthermore, stimuli-responsive LIS were reported, allowing static and dynamic wetting properties of the surface to be adapted in response to external stimuli (Lou et al. 2020).

3. Single-phase flow along LIS

3.1 Effective slip length of LIS

While for superhydrophobic surfaces usually the viscous dissipation in the gas phase enclosed in the indentations of the surface can be neglected, the effect of the lubricant plays a key role for the drag force experienced by a liquid flowing along a LIS. It is customary to characterize the drag by an effective slip length β_{eff} defined via

$$u\big|_{y=0} = \beta_{\text{eff}} \left.\frac{\partial u}{\partial y}\right|_{y=0}, \qquad 1$$

where the flow direction at the surface is *x*, *y* is the coordinate normal to the surface, and *u* is the flow velocity magnitude. By convention, the surface is located at $y = 0$. Specifically, Equation 1 refers to a scenario where at a distance y_0 away from the surface (large compared to the typical scale of the surface features), the flow field looks like a Couette flow. Extrapolating this flow field to the plane of the surface yields a non-vanishing flow velocity at $y = 0$ from which the effective slip length can be read off using Equation 1. Importantly, this equation does not refer to the (usually quite complex) actual flow field, but to the Couette flow as defined above. The effective slip length needs to be distinguished from the intrinsic slip length of a liquid on a flat solid surface, which is often of the order of nanometers. For example, measurements of the intrinsic slip length of water on hydrophilic surfaces give values below 10 nanometers (Lei et al. 2016).

Assuming a vanishing intrinsic slip length, on a SHS the interface at the surface is composed of solid-liquid patches with vanishing slip and gas liquid patches with vanishing

shear stress. The liquid-liquid patches on a LIS form the analog of the gas-liquid patches of a SHS. The shear stress on these patches does not vanish, but depends on the viscosity of the lubricant and on the flow pattern inside the surface indentations. For these reasons, it is very difficult to obtain closed-form mathematical expressions for the effective slip length. The fact that the lubricant will be displaced from the indentations, as discussed in section 3.2, introduces further complications. In the following, the ideal case of a flat liquid-liquid interface will be discussed.

One of the early attempts to study the influence of the flow inside the indentations of a surface was made by Hocking (1976), who considered transverse flow over an array of infinitely thin parallel plates. In this study, two immiscible fluids of identical viscosity were assumed. In this and the following, the terms “transverse” and “longitudinal” refer to flow normal to and along the orientation of surface corrugations. An important distinction has to be made concerning the connectivity of the space in which the lubricant is confined. For surfaces with grooves, this space is usually disconnected, i.e. the lubricant flow within a specific groove is not coupled to the flow inside the other grooves. By contrast, for a surface with pillars, this space can be viewed as a porous medium with connected pores, and results obtained for flow inside porous media can be applied. Along these lines, Ybert et al. (2007) suggested an expression for the effective slip length on a surface with pillars and found good agreement with finite-element calculations. The extreme case of this scenario, i.e. a situation in which the volume fraction of the pillars is so small that they can be neglected in comparison to the lubricant-filled domain, was considered by Busse et al. (2013).

Generally, a local slip length value can be assigned to a specific point at the liquid-liquid interface when replacing the model velocity field of Equation 1 (Couette flow) by the local flow field at this point. It is important to note that LIS cannot simply be modeled by averaging the slip length over the liquid-liquid interface and working with this average value, while a vanishing slip length is assigned to the solid-liquid interface patches. This is explained

by the fact that the local slip-length values depend on the angle between the flow velocity and the orientation of the surface structures (Nizkaya et al. 2014). For surfaces with parallel grooves, Schönecker et al. (2014) provided closed-form analytical expressions for the effective slip length in the case of longitudinal and transverse flow at low Reynolds numbers. These expressions are valid for arbitrary viscosity ratios of the two liquids and for arbitrary values of the parameters characterizing the surface geometry.

Experimental studies of slip on LIS are so far rather scarce. An early study was conducted by Solomon et al. (2014), using a cone-and-plate rheometer to determine the effective slip length on a microstructured surface with an array of posts. The results are roughly consistent with the predictions of Ybert et al. (2007). Especially, it was found that the slip length increases as the viscosity ratio between the working fluid and the lubricant increases. The slip length on an unstructured surface completely wetted by a thin silicone oil was determined based on colloidal probe atomic force microscopy (Scarratt et al. 2020). The results give indications that there could be a nonzero slip length at the interface between the two immiscible liquids, a sucrose solution and silicone oil as lubricants. Slip at liquid-liquid interfaces could add to the drag reduction properties of LIS.

3.2 Drainage, stability and structure formation of the lubricant under shear

Compared to SHS, LIS possess self-healing properties, which means that when the lubricant becomes locally displaced from a surface, capillary forces will replenish the liquid and (approximately) restore the original structure of the surface. However, this desirable feature comes at a cost: It is much easier to displace the lubricant by exerting shear forces on the surface than to displace the gas from the indentations of a SHS. The reason is that liquids have a much higher dynamic viscosity than gases. The higher level of viscous stresses makes it easier to deform a fluid interface, which is the prerequisite for displacing the lubricant.

A prototypic study of the shear-driven failure of liquid-infused surfaces was conducted by Wexler at al. (2015a). A microfluidic flow cell was used with streamwise parallel grooves at the bottom, filled with silicone oil stained with a fluorescent dye (Figure 3a). The green fluorescent silicone oil fills 50 parallel grooves and is imaged in top view (Figure 3b). When a threshold flow rate is exceeded, drainage of silicone oil is observed (Figure 3c) up to a point where a steady-state configuration is reached. Figure 3d shows the structure of the grooves. Wexler el al. (2015a) were able to formulate a theoretical model for the steady-state length L_∞ that compares favorably to experimental data. This model was later extended to account for the viscosity ratio between the working fluid and the lubricant (Liu et al. 2016). The drainage of grooves can cause so-called overflow cascades: The lubricant displaced from the grooves forms bulges that merge and from drops that cover the LIS (Jacobi et al. 2015).

A suitable principle to prevent drainage of grooves is to create liquid-infused regions that have an extension smaller than L_∞. This has been achieved by patterning a periodic array of hydrophilic stripes orthogonal to the grooves (Figure 3e and f) (Wexler at al. 2015b). These stripes are preferentially wetted by the working fluid rather than by the lubricant. The lubricant inside a groove then forms disconnected volumes separated by hydrophilic stripes (Figure 3f). In a situation where the lubricant is almost completely drained from a groove without stripes, the hydrophilic stripes ensure that the liquid is largely retained inside the grooves (Wexler at al. 2015b).

While the drainage of the lubricant has been studied quite intensely for the case of longitudinal flow over parallel grooves, studies on the shear-induced failure for other surface textures or flow configurations appear to be scarce. There are some computational fluid dynamics studies on the stability of the liquid-liquid interface for the case of transverse flow over parallel grooves, yielding a stability map in terms of the capillary number and the viscosity ratio (Ge et al. 2018).

The (partial) drainage of the lubricant by shear flow is one example of a more general phenomenon: The flow pattern inside the working fluid sculpts the distribution of the lubricant, which, in turn, influences the flow in the working fluid. Flow patterns can spontaneously form by self-organization in systems that exhibit hydrodynamic instabilities. Two classical examples of such instabilities are the Bénard-Marangoni (Davis 1987, Schatz & Neitzel 2001) and the Faraday instability (Miles & Henderson 1990). The Bénard-Marangoni instability was studied for the case that the liquid layer is separated from the solid surface by a thin lubrication film (Nejati et al. 2015). The corresponding setup is sketched in Figure 4a. The presence of the thin lubrication film shifts the marginal stability point of the upper liquid to smaller values of the critical Marangoni number. Furthermore, the flow pattern in the convection cells (drawn schematically in Figure 4a) sculpts the lubrication film. This is visible in Figure 4b. The figure shows a top view, with the well-known hexagonal convection cells well visible. At the center of each cell, there is a bright spot, which is caused by a bulge of the lubrication film, induced by shear forces due to the flow in each cell. There is a one-to-one correspondence between the pattern of convection cells and the deformation pattern of the lubrication film. A similar sculpting of a thin lubrication film under a thicker liquid layer is observed in the self-organization process via the Faraday instability (Zhao et al. 2019). Figure 4c shows a schematic of the corresponding experimental setup. The system of two superposed liquids sits on a horizontal harmonically vibrating surface. Similar to the case of the Bénard-Marangoni instability, the lubrication film shifts the point of marginal stability. Although the flow velocity in the upper layer is virtually reversed (see the sketch in Figure 4c) each half period, remarkably, a steady-state deformation in the lubrication layer builds up (Figure 4d). This nonlinear response of the system can be qualitatively explained by the nonlinearities due to the liquid-liquid interface. Figure 4d shows a superposition of two snapshots, the light reflections from the surface of the upper layer (two nested square arrays of bright spots) and an image showing the lubrication layer. In the latter, the dark regions are those in which the

lubrication film is thinned by shear forces. The superposition of the two images shows that there is a one-to-one correspondence between the deformation pattern of the upper liquid layer and that of the lubrication layer

3.3 Drag in turbulent flow

In many industrial applications, turbulent flows occur. In that context, in the past decade especially SHS were studied as candidate structures that reduce hydrodynamic drag (Golovin et al 2016). Turbulent flow poses significant challenges to SHS. For example, pressure fluctuations can induce the Cassie-to-Wenzel wetting transition, which is difficult to reverse (Manukyan et al. 2011, Papadopoulos et al. 2013, Rofman et al. 2020). Compared to that, LIS are significantly more robust owing to their self-healing.

Some basic features of LIS concerning drag reduction in turbulent flow in comparison to superhydrophobic surfaces were experimentally confirmed by Rosenberg et al. (2016). They used a Taylor-Couette apparatus to measure the drag reduction factor. As expected, the achievable drag reduction depends on the viscosity ratio between the working fluid and the lubricant. LIS were found to be superior to superhydrophobic surfaces that suffered from a partial transition between the Cassie-Baxter and the Wenzel state. In subsequent work, a drag reduction of up to 35 % was measured using a LIS in a Taylor-Couette apparatus (van Buren & Smits 2017).

Conceptually, for turbulent flow over LIS it is a priori unclear what the relevance of the effective slip length discussed in Section 3.1 is. The reason is that β_{eff} is a useful concept only on a scale significantly larger than the characteristic feature size of the LIS, and the latter needs to be compared to the viscous length scale of the turbulent flow, given by $\nu\left(\rho/\tau_{\mathrm{w}}\right)^{1/2}$, where ν is the kinematic viscosity, ρ is the density and τ_{w} is the wall shear stress. For the case that the viscous length scale is smaller than β_{eff}, the usual assumption underlying most

models for the effective slip length, namely Stokes flow in the boundary region, breaks down. Therefore it is useful to define a dimensionless effective slip length via

$$\beta_{\mathrm{eff}}^{+} = \frac{\beta_{\mathrm{eff}} \tau_{\mathrm{w}}^{1/2}}{\nu \rho^{1/2}} \qquad 2$$

and to keep in mind that there will be a threshold value of β_{eff}^{+} above which the slip length derived from Stokes flow ceases to be a useful concept when considering turbulent flow. In comparison to the predictions from Schönecker et al. (2014), the numerical simulations reported in (Fu et al. 2017) indicate that this threshold value is about 5 for lubricant-filled longitudinal grooves.

Direct numerical simulations of turbulent flow over LIS have been performed for a number of different surface topographies, among others for the standard textures of parallel grooves (Fu et al. 2017, Chang et al. 2019, Arenas et al. 2019) and arrays of posts (Arenas et al. 2019). Some of the results significantly deviate from the predictions obtained for Stokes flow along LIS. Figure 5a shows the drag reduction due to a textured surface relative to a smooth, flat surface (Arenas et al. 2019) as a function of the viscosity ratio N between the working fluid and the lubricant. Turbulent flow between two parallel plates (one of them being textured and liquid-infused) was considered, with a flat, undeformable liquid-liquid interface. The different curves represent different surface textures.

At least two aspects of these results defy intuition gained from Stokes flow. First, the drag reduction can be negative, meaning that the drag of a LIS is larger than that of a flat no-slip surface. Second, even at $N \approx 1$ a significant drag reduction may be achieved. This is counter-intuitive, because for $N = 1$ the flow configuration is similar to single-phase flow over a textured surface. For the latter, numerical computations performed for surfaces decorated with staggered cubes, for example, suggest that for configurations comparable to the one with higher liquid-liquid area fraction shown in Figure 5a, the drag increases (Leonardi & Castro 2010). Qualitatively, the drag reduction of LIS for $N \approx 1$ can be

explained by considering the time-averaged secondary flow above a textured surface. Corresponding streamlines for single-phase flow along longitudinal grooves are shown in Figure 5b (Arenas et al. 2019). It can be seen that the secondary flow penetrates into the grooves. By contrast, the liquid-liquid interface of LIS tends to damp the wall-normal fluctuations and to keep the streamwise secondary vortices above the cavities. This reduces the momentum transfer inside the cavities and results in drag reduction.

4. Drops on liquid-infused surfaces

4.1 Static wetting

A drop on a LIS has a wetting ridge (Figure 6), which complicates the concept of a contact angle. There can be a solid three-phase contact line where the substrate, drop and lubricant (i.e. infused liquid) meet, a liquid three-phase contact line at the top of the wetting ridge where gas, drop and lubricant meet, both types or none at all depending on the interfacial tensions (Schellenberger et al., 2015). For a completely submerged texture there is no solid three-phase contact line whilst for a cloaked drop there is no liquid three-phase contact line. Nonetheless, an apparent contact angle, θ_{app}, can be defined at the inflection point in the profile of the drop at the top of the wetting ridge (Guan et al., 2015). There are also three Neumann angles, θ_D, θ_G, and θ_L, related to the interfacial tensions by $\gamma_{LD}/\sin\theta_G=\gamma_{DG}/\sin\theta_L=\gamma_{LG}/\sin\theta_D$.

Semprebon et al. (2017) considered the apparent contact angle for a drop with wetting ridges controlled by the film and drop Laplace pressures, ΔP_{LG} and ΔP_{DG}, related to lubricant and drop volumes, and derived a closed-form equation for the apparent contact angle. Here we interpret their results using an effective interfacial tension, $\gamma_{LIS]f}$, between the liquid infused surface and an immiscible fluid, *f*. Regarding a LIS to be composed of a solid surface fraction, φ_s, and an infused-liquid surface fraction (1-φ_s), we define a Cassie-Baxter

combination $\gamma_{[LIS]f} = \varphi_S\gamma_{Sf} + (1-\varphi_S)\gamma_{Lf}$, where γ_{Sf} and γ_{SL} are the solid-fluid and liquid-fluid interfacial tensions, and f can be gas/air/vapor (G), water/drop (D) or lubricant/infused liquid (L) (see also Sadullah, et al., 2020a). The definition of $\gamma_{[LIS]f}$ can also be generalized to Cassie-Baxter-Wenzel combinations of the two interfacial tensions allowing different surface fraction and roughness parameters for the LIS interface with different fluids. When φ_s=0 the surface has a continuous lubricant film in contact with a fluid, f, even when there is an underlying texture. In the limit of a vanishingly small wetting ridge, corresponding for most LIS to large and negative lubricant pressure compared to the Laplace pressure in the water drop (i.e. $-\Delta P_{DG}/\Delta P_{LG} \rightarrow 0$), the apparent contact angle θ^S_{app} is,

$$\cos\theta^S_{app} = \frac{\gamma_{[LIS]G} - \gamma_{[LIS]D}}{\gamma_{Eff}} \qquad 3$$

Equation 3 can also be derived from interfacial force balance or minimizing surface free energy changes at the drop periphery (Kreder et al., 2018; McHale et al., 2019). The limit of a smooth solid surface $\varphi_s \rightarrow 1$, gives Young's law, $\cos\theta^S_{app} \rightarrow \cos\theta_{DS(G)} = \frac{\gamma_{SG} - \gamma_{SD}}{\gamma_{DG}}$, which defines the contact angle of a drop on the solid in gas $\theta_{DS(G)}$. The limit of a continuous thin liquid layer $\varphi_s \rightarrow 0$, gives a liquid form of Young's law, $\cos\theta^S_{app} \rightarrow \cos\theta_{DL(G)} = \frac{\gamma_{LG} - \gamma_{LD}}{\gamma_{Eff}}$, not involving interfacial tensions linked to the underlying solid texture, and defines a drop contact angle on the lubricant in gas $\theta_{DL(G)}$. In this limit, drop behavior on an ideal ultra-smooth hysteresis-free "solid" surface can be studied (e.g. McCarthy et al., 2019; Ruiz-Gutiérrez et al., 2017; Wells et al., 2018). Using Cassie-Baxter weighted combinations of a drop wetting the solid and lubricant components of the texture, Equation 3 gives $\cos\theta^S_{app} = \varphi_S\cos\theta_{DS(G)} + (1-\varphi_S)\cos\theta_{DL(G)}$.

Based on Semprebon et al. (2017), for small $-\Delta P_{DG}/\Delta P_{LG}$ the apparent contact angle can be found from

$$\frac{\gamma_{[LIS]D}-\gamma_{[LIS]L}-\gamma_{LD}\cos(\theta_{app}-\theta_D)}{\gamma_{[LIS]G}-\gamma_{[LIS]L}+\gamma_{LG}\cos(\theta_{app}+\theta_G)} = 1-\alpha\left(\frac{\Delta P_{DG}}{\Delta P_{LG}}\right), \quad 4$$

where α=½ for an axially symmetric droplet (Semprebon et al., 2021). In contrast to Young's law, the apparent contact angle on a LIS depends on the material constants and the size of the wetting ridge relative to the size of the drop. Increasing -$\Delta P_{DG}/\Delta P_{LG}$ increases the ridge height around a drop and causes a rotation of the Neumann triangle decreasing the apparent contact angle (Figure 6b). Experimentally, the ratio of pressures can be determined from the lubricant-vapor and lubricant-drop interface curvatures and interfacial tensions. Equation 4 gives the linear correction to the vanishing ridge height solution, i.e. $\cos\theta_{app} = \cos\theta_{app}^{S} - \frac{\alpha\Lambda}{\gamma_{DG}}\left(\frac{\Delta P_{DG}}{\Delta P_{LG}}\right)$, where $\Lambda = \gamma_{LG}\cos\left(\theta_{app}^{S}+\theta_G\right)+\gamma_{[LIS]G}-\gamma_{[LIS]L}$. Physically, the rotation angle is the ratio of ridge height to drop base radius (Kusumaatmaja et al., 2021). Similar concepts of contact line ridges and rotation of the Neumann triangle occur for drops on liquid films on flat surfaces (Tress et al., 2017) and soft solid substrates (Karpitschka et al., 2015, 2016) (for a review of soft wetting see Andreotti & Snoeijer, 2020; Bico et al., 2018).

4.2 Onset of drop motion

Setting a drop into motion involves concepts of static and kinetic friction analogous to those for solids (Gao et al., 2018). On a smooth solid surface, the work done in moving a drop forwards by wetting a new surface of width, w, and length, Δl, at its front and dewetting at its rear is $\gamma_{DG}(\cos\theta_R - \cos\theta_A)w\Delta l$, where θ_A and θ_R are the advancing and receding contact angles, respectively (Furmidge, 1962). The resultant pinning force $F_p=\gamma_{DG}(\cos\theta_R - \cos\theta_A)w$, can be approximated as $F_p=-w\gamma_{DG}\sin\theta_S\Delta\theta_{CAH}$ where $\Delta\theta_{CAH}=\theta_A-\theta_R$ and θ_S is the static contact angle (Barrio-Zhang et al., 2020). For a LIS, $F_p=-\Delta\theta_{CAH}F_N/\pi$ where the normal capillary force is $F_N=\pi w\gamma_{Eff}\sin\theta_{app}$, which is reminiscent of Amonton's first two laws of solid friction, but with a coefficient of static friction $\mu_s= \Delta\theta_{CAH}/\pi$. By analogy, the coefficient of kinetic friction is proportional to the difference between the front and rear contact angles of a moving drop.

Simulations of drop depinning using a post model suggest there are two types of processes on a LIS (Sadullah et al., 2020b). Lubricant at the rear of each ridge at the front and back of a drop bridges to the next post, i.e. $\theta_{L[LIS](f)} = 0$ where the contact angle for lubricant on a LIS in the presence of a fluid (*f*=drop or gas) is defined as $\cos\theta_{L[LIS](f)} = \frac{\gamma_{[LIS]f} - \gamma_{[LIS]L}}{\gamma_{Lf}}$. At the front of these ridges, lubricant detaches from the top of a post and slides when the contact angle satisfies $\cos\theta_{L[LIS](f)} = \phi_S \cos\theta_{L[LIS](f)} + (1 - \phi_S)$ where ϕ_S is the line (rather than area) average of the solid surface fraction. This gives a net pinning force per unit length $f_p = \phi_S\left[\gamma_{LD}\left(1 - \cos\theta_{L[LIS](D)}\right) + \gamma_{LG}\left(1 - \cos\theta_{L[LIS](G)}\right)\right]$ independent of the interfacial tension between the drop and gas. This allows advancing and receding contact angles for a drop to be defined and a sliding angle to be predicted (Sadullah et al., 2020b; Semprebon et al., 2017).

LIS allow the design of slippery surfaces with low contact angle hysteresis and low apparent contact angles whilst retaining a large drop footprint. For example, Luo et al. (2017) have shown momentum can be transferred to a drop from a surface acoustic wave to actuate low friction motion, whilst maintaining a large contact area for sensing. Since liquid adhesion of a drop to a surface depends on the receding contact angle, the combination ($\theta_R \approx \theta_{app}$, $\Delta\theta_{CAH}$) defines how easily a drop can be moved along a surface (shear hydrophobic) and removed perpendicularly from the surface (tensile hydrophobic) (Gao & McCarthy, 2008; Tao et al., 2020). Thus, an inverted LIS may easily shed a hanging drop through motion along its surface, but still adhesively retain the drop despite gravity (Eifert *et al*, 2014; Launay et al., 2020).

Surfaces can be viewed as more/less wettable as defined by the contact angle of a drop on a solid, $\theta_{DS(G)}$, or by the contact angle of a drop on the lubricant, $\theta_{DL(G)}$. When a drop rests on the top of a post-type model textured surface with gaps between the posts filled either by a lubricant or by a gas, the apparent contact angle can be described by a Cassie-Baxter equation,

$\cos\theta_{app}^{S} = \varphi_{Top}\cos\theta_{Top} + \left(1 - \varphi_{Top}\right)\cos\theta_{In-fill}$. When the top of posts do not have a conformal lubricant coating and the drop is in direct contact with the underlying solid $\varphi_{Top}=\varphi_{S}$. However, when the top of the posts have a lubricant conformal coating of thickness ε preventing direct contact by the drop $\varphi_{Top}=\varphi_{S}+2\varepsilon$. Thus, self-propelled drop motion on conformally-coated lithographic rails whose width narrows along their length and where the gaps contain air, is towards the direction with a greater fraction of tops of the rails (Launay *et al*, 2020). In contrast, drop motion on a surface composed of gradient-width rails which have no lubricant on their tops, but have a lubricant in their gaps, can be in either direction depending on the sign of ($\cos\theta_{DS(G)}$-$\cos\theta_{DL(G)}$) (Figure 7a,b) (Sadullah et al., 2020a). In all cases, motion is towards the area with greater wettability. Similar concepts apply to other forms of self-propelled drop and bubble motion on structures with wetting gradients and lubricants, such as condensing drops on slippery asymmetric bumps (Park et al, 2016), drops on liquid filled wedge textures (Figure 7c) (Zheng et al., 2017) and bubble transport (Zhang et al., 2018).

A Wenzel equation for slippery conformal-coated surfaces can also be defined, $\cos\theta_{app}^{S} = r_{W}\cos\theta_{L}$ where r_W is the Wenzel roughness at the drop periphery. Slippery Wenzel states with micro-grooves have been used for nucleation and directional transport of water drops (Dai et al., 2015). We also envision more complex combinations of roughness and surface fractions with conformal coatings modelled through a series of transformations $\theta_S \rightarrow \theta_L \rightarrow \theta_W \rightarrow \theta_{CB}$ where the first transformation is the conformal lubricant coating and the second and third introduce local Wenzel roughness and solid/lubricant Cassie-Baxter surface fractions (Shirtcliffe et al., 2010). Beyond roughness and topography, apparent contact angles on LIS can be used more widely in wetting problems, e.g., electrowetting (Brabcova et al., 2017; Hao et al., 2014; McHale et al., 2019).

4.3 Drop dynamics

Studies of the mobility of drops on LIS have typically used tilted substrates and related the velocity of drop motion, U, to the body force, F. Due to the four-phase system and the textured surface, there is a rich variety of sources of viscous dissipation, including in the drop, lubricant film and wetting ridge (Figure 8a). Moreover, drop motion can dynamically shape the ridge and film thickness (Figure 8b). To understand the viscous dissipation, it is necessary to consider the viscosities of the drop and lubricant, the height and density of the physical texture (assumed here to be pillars), the lubricant film thickness and shape of the wetting ridge, including any dynamic effects. Experiments have reported different regimes dependent on the drop-lubricant viscosity ratio and capillary number. For viscous drops compared to the lubricant viscosity, drop velocity follows a Stokes-type law scaling linearly with force and inversely with drop viscosity. For non-viscous drops, regimes include velocity scaling linearly with force and inversely with lubricant viscosity, non-linearly with a 3/2 power law and a texture dependence, and (at the highest capillary numbers) a cubic power law independent of texture density. Drops undergo rolling (Figure 8c) and may undergo a combination of rolling and sliding.

Smith et al. (2013) measured drop-shedding velocities on tilted liquid infused nano-grass topped micro-post surfaces. By matching the shear stress at the drop-lubricant interface they deduced an interfacial velocity, U_i, scaling as $U_i/U \sim \left(1 + \frac{\eta_L h_{CM}}{\eta_D d}\right)^{-1}$, where h_{CM} is the drop centre of mass and d is the lubricant film thickness. They predicted their low viscosity drops ($\eta_D < \eta_L$) followed a rolling motion consistent with the observed trajectories of particles added to the drops. They also estimated the rate of viscous dissipation in the bulk drop, lubricant film and the wetting ridge and concluded that dissipation from the wetting ridge dominated. Importantly, the resulting scaling of drop velocity inversely proportional to lubricant viscosity was consistent with their data (also confirmed by Eifert et al. 2014).

However, the predicted velocity-force scaling was Stokes-like $U \sim \frac{F}{\eta_L}$, but published data deviates from linearity at higher tilt angles.

Daniel et al. (2017) probed the dynamical states of the lubricant film at a resolution down to a few nanometers using thin-film interference. This revealed oleoplaning on continuous films of lubricant for drops moving on micropost textured LIS that, under static conditions, had completely or partially wetted tops. The film thickness, h, increased with velocity and followed a Landau-Levich-Derjaguin (LLD) scaling as $h \sim R\mathrm{Ca}^{2/3}$ (e.g. see Seiwert et al., 2011), where R is drop radius and the capillary number is $\mathrm{Ca}=\eta_L U/\gamma_{DL}$, provided it was larger than the height of the microposts, h_p. Using a cantilever force sensor they measured velocity-force relationships and fitted their data to $U \sim F^{3/2}$ and $U \sim F$, for films with height $h=h_{LLD}$ and $h_{LLD}=h_p$, respectively. They described the functional form of these relations using a LLD mechanism (Daniel et al., 2018, 2017). In their model, the dissipation in the rear corner of the front ridge is determined by a deformation over a distance $l \sim R\mathrm{Ca}^{1/3}$ leading to a lubricant film thickness $h_{LLD} \sim R\mathrm{Ca}^{2/3}$ where the capillary number is $\mathrm{Ca}=\eta_L U/\gamma_{LD}$. Since force is the viscous stress $\eta_L U/h_{LLD}$ integrated over the transition region area $2\pi Rl$, the velocity and lubricant viscosity scaling is $U \propto F^{3/2}/\eta_L$ provided $h_{LLD}>h_p$. In these experiments, the lubricant is more viscous than the drop ($\eta_D<\eta_L$) and the drop rolls whilst oleoplaning (Figure 8d). Similarly to Smith et al. (2013) viscous dissipation occurs in the ridge, but here it is modelled as occurring at the rear of the ridge in a small dynamically shaped transition region whose height and extent depends on the drop velocity. In subsequent work, these ideas where developed and the impact on the thickness of the cloaking of the drop and depletion of lubricant as the ridge grows were identified (Kreder *et al*, 2018).

Keiser et al. (2017) studied drop shedding on tilted pillar-based micro textures with and without a hydrophobic nanoparticle coating with both large and small drop-lubricant viscosity ratios and with modest slip ($U_i/U<0.1$). Their data and analysis suggested that there

is a crossover from bulk drop to a lubricant ridge-dominated dissipation regime with viscosity ratio. When $\eta_L < \eta_D$ the dissipation for a millimetre-size drop was Stokes-like with a linear velocity-force relationship and was inversely proportional to drop viscosity, i.e. $U \sim \frac{F}{\eta_D}$. In the opposite limit when $\eta_L > \eta_D$, dissipation was modelled as dependent on texture density and mainly occurred in a dynamically shaped ridge with a dynamic contact angle at its front corner. Taking into account Tanner's law for the dynamic contact angle, $U \sim \frac{\gamma_{LG}\theta^3}{\eta_L}$, and the scaling of the wedge friction which occurs over the pillar tops, $\sim \frac{\varphi_S R \eta_L U}{\theta}$, gives a velocity-force relationship that retains Smith et al's (2013) inverse scaling with lubricant viscosity but has a 3/2 power law, $U \sim \frac{F^{3/2}}{\eta_L \, \gamma_{LG}^{1/2} \, R^{3/2} \, \varphi_S}$. At higher driving forces, and hence higher capillary numbers, they observed a transition to a texture-density independent cubic-law regime $U \sim F^3/\eta_L$, interpreted tentatively as a self-lubrication effect due to a fully dynamic meniscus. This was assumed to occur across a dynamic meniscus of unknown size r_{men} and creating a thick lubricant film obeying a LLD thickness scaling $h_{LLD} \sim r_{men}(\eta_L U/\gamma_{LD})^{2/3}$. However, at these higher velocities, there is insufficient detail on the existence and shape of any dynamic meniscus, the nature of the lubricant film, and data to have clarity on a scaling law (Keiser, 2020).

Lattice-Boltzmann simulations have been able to reproduce the crossover (at around $\eta_D \sim 2\eta_L$) between the bulk drop and ridge dominated energy dissipation regimes (Sadullah et al., 2018). These simulations focused on partial wetting liquids also highlighted the relative importance between contact line pinning and viscous dissipation, and the role of the lubricant contact angle in determining the aspect ratio of the ridge. For large apparent contact angles, contact line pinning dominates and drops on more wetting lubricants move faster, whereas for small apparent contact angles, viscous friction in the ridge dominates and drops on less wetting lubricants move faster. The reduction in the velocity of drops on LIS with reducing

apparent contact angles due to reducing interfacial tension using ethanol-water mixtures has been reported by Sharma et al. (2019).

It has also been suggested that the 3/2 power law is universal for drops whose viscosity is less than the lubricant film viscosity and can fit the entire data set in Daniel et al. (2017), i.e. both for films with height $h=h_{LLD}$ and $h=h_p$ (Keiser et al., 2020). We note that a 3/2 power law can also be fitted to the data in Smith et al. (2013). Keiser et al.'s interpretation identifies dissipation mechanisms in the front and rear corners within the dynamically shaped wetting ridges (regions 1 and 3, and regions 2 and 4 in Figure 8a). The dissipation in the front corners of the two ridges is determined by a dynamic contact angle (visualized in Figure 8b) and so has a velocity scaling inversely in lubricant viscosity, i.e. $U \sim \frac{F^{3/2}}{\eta_L \, \gamma_{Lf}^{1/2} \, R^{3/2} \, \varphi_S}$ where γ_{Lf} is γ_{LG} or γ_{LD} for the front and rear ridges, respectively. (Keiser et al., 2020, 2017). This means that drop friction from these two front corners are always present and tuned by choice of solid surface fraction (i.e. pillar density in a micro-texture). The dissipation from the rear corners is determined by an LLD coating mechanism with a deformation of the rear of the foot of each ridge over a distance $l \sim R\mathrm{Ca}^{1/3}$ leading to a lubricant film thickness $h_{LLD} \sim R\mathrm{Ca}^{2/3}$ where the capillary number is either $\mathrm{Ca}=\eta_L U/\gamma_{LD}$ (region 2) or $\mathrm{Ca}=\eta_L U/\gamma_{LG}$ (region 4). This results in a lubricant scaling in each region of $U \propto F^{3/2}/\eta_L$ with pre-factors $\frac{1}{\gamma_{LD}^{1/2} R^{3/2}}$ and $\frac{1}{\gamma_{LG}^{1/2} R^{3/2}}$ for the rear corners of the front and rear ridges, respectively. Here an LLD film is only expected on a micro-post texture when the pillar height, h, is less than h_{LLD} or, equivalently, the drop velocity exceeds $U^* \sim \left(\frac{\gamma_{Lf}}{\eta_L}\right)\left(\frac{h}{R}\right)^{3/2}$. Otherwise, there is no LLD film and the friction in regions 2 and 4 is negligible compared to that in regions 1 and 3. Thus, dissipation at the front of ridges always occurs, whilst at their rear, dissipation can be switched on and off by varying pillar height h_p or drop velocity U, whilst the scaling remains $U \propto F^{3/2}/\eta_L$ (Figure 8e). The drop

speed threshold, for a given height of pillars, at which the LLD film is established, depends on texture density, but thereafter the resulting friction is independent of the texture density.

ACKNOWLEDGEMENTS

We are grateful to colleagues and coworkers for exchanges of ideas on LIS and suggestions to improve the manuscript. Particular thanks are due to Tobias Baier, Armelle Keiser, Halim Kusumaatmaja, Rodrigo Ledesma-Aguilar, Ciro Semprebon and Gary Wells. Thanks to Muhammad Sadullah for assistance with Figure 6 and to Joanna Aizenberg, Jiang Cheng, Dan Daniel, Armelle Keiser, Gareth McKinley, Howard A. Stone, Kripa Varanasi, Jason S. Wexler, and Yanfen Zheng for providing original figures.

SUMMARY POINTS

1. Owing to their robustness and self-healing properties, LIS represent a promising alternative to superhydrophobic surfaces for applications involving either single-phase flow or droplet transport along surfaces. However, the shear-induced failure is an important effect limiting the usefulness of LIS interacting with a flow field. Special measures can be taken to suppress the shear-induced failure.
2. One key quantity characterizing LIS is the effective slip length, which, different from superhydrophobic surfaces, depends on the flow field in the fluid-filled indentations of the surface. Slippery LIS can reduce drag even under turbulent conditions.
3. Flow fields interacting with LIS can sculpt the lubricant layer, which, in turn, affects the flow field.
4. Drops on LIS have a wetting ridge and an apparent contact angle, which for vanishingly thin lubricants obeys a liquid form of Young's law. For increasing ridge height, this contact angle decreases by rotation of a Neumann triangle.
5. Friction for drops moving on LIS depends on the viscosity ratio and properties of the physical texture. For viscous drops, dissipation occurs in the drop and its velocity obeys $U \sim F/\eta_D$. For non-viscous drops, dissipation occurs in dynamically shaped wetting ridges and drop velocity obeys power-laws $U \sim F^n/\eta_L$.

FUTURE ISSUES

1. The widespread use of LIS could be promoted by a better understanding of the shear-induced failure and by developing surface designs allowing this failure mechanism to be suppressed.
2. The sculpting of the lubricant layer holds promise for creating surface structures by self-organization and for the control of flow fields via their interaction with the surface.
3. Textured surfaces with two or more different lubricants and stimuli-responsive LIS could widen the range of applications involving flow and drop transport along LIS.
4. For motion of non-viscous drops (relative to lubricant viscosity), what is the mechanism and nature for deviation from a universal $U \sim F^{3/2}$ power law at higher capillary numbers?

Figures

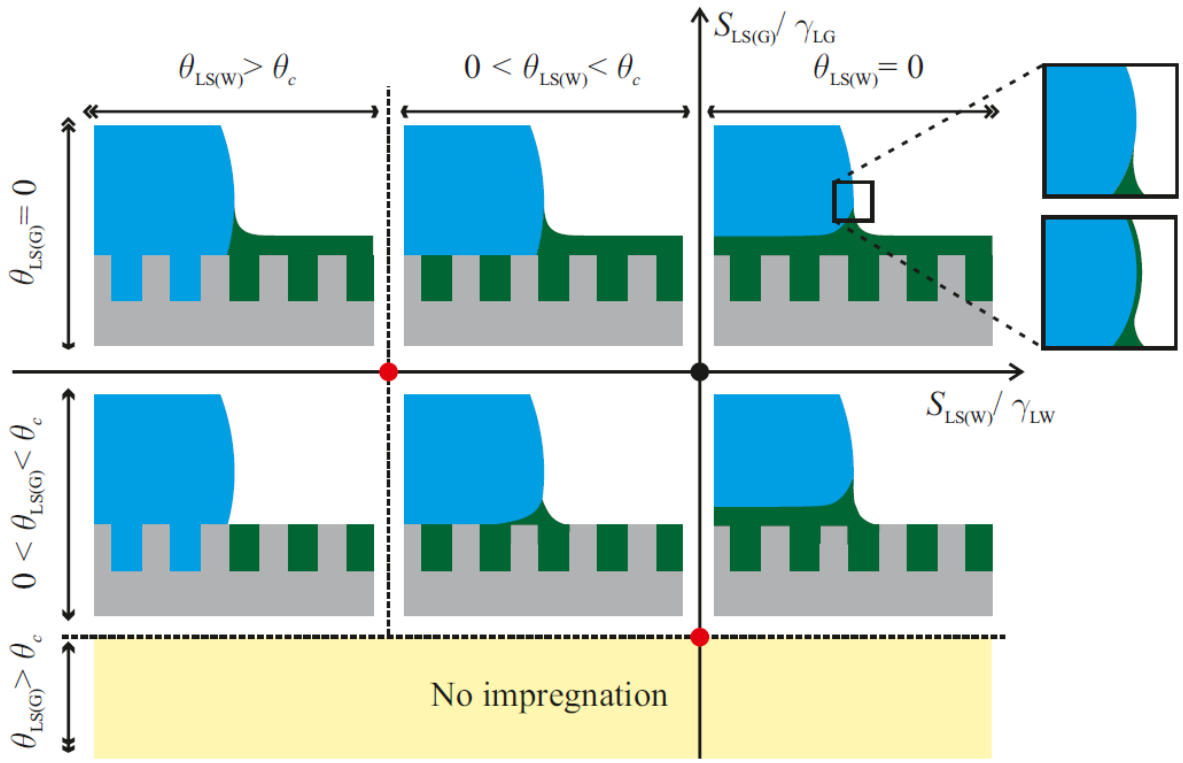

Figure 1: Map showing the possible wetting morphologies when a drop wets a LIS. The *x*- and *y*-axis measures the dimensionless spreading coefficient $S_{LS(W)}/\gamma_{LW}$ and $S_{LS(G)}/\gamma_{LG}$ respectively. The spreading coefficients can be translated into contact angles, as indicated in the figure. The origin of the coordinate system is marked by the red dot. The black dots mark points that are a distance of $(r-1)/(r-\phi)$ away from the origin. Liquid-infused surfaces exist everywhere above the dashed horizontal line. Below that line, the state of lowest energy is a dry surface. Each of the six different wetting morphologies sketched in the figure comes in two different versions, depending on whether or not the lubricant cloaks the water surface. Cloaking requires a positive spreading coefficient of lubricant on water. Adapted with permission of the Royal Society of Chemistry from (Smith et al. 2013); permission conveyed through Copyright Clearance Center, Inc.

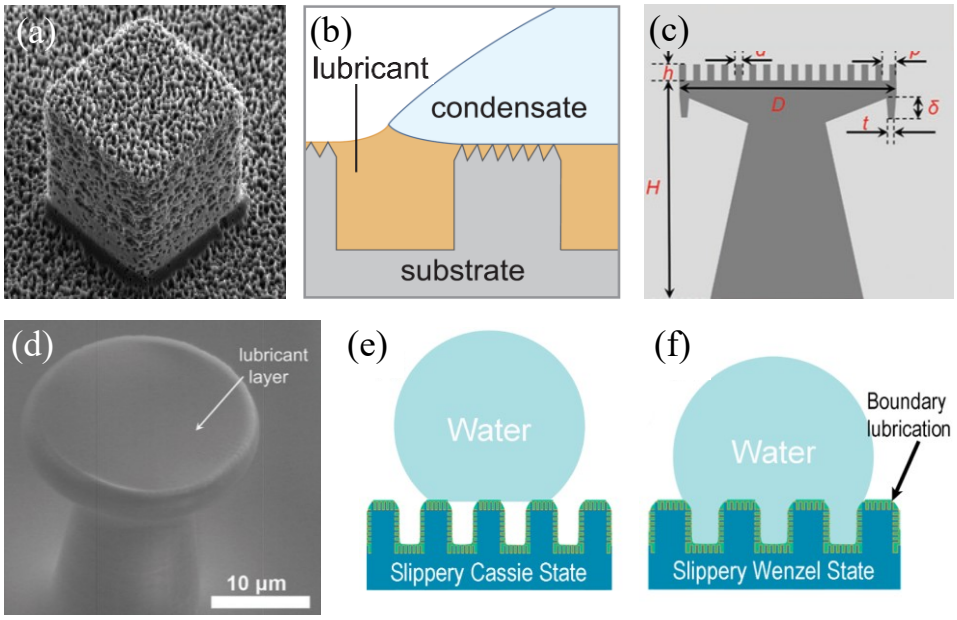

Figure 2: Hierarchical LIS. (a) Single micro-post with etched nano-grass structures. (b) Schematic of a drop on liquid-infused nano-grass microstructures. (c) Schematic of a doubly re-entrant micro-pillar. (d) SEM image of such a pillar with lubricant coating. (e) and (f) are schematics showing a drop on conformally coated microstructures in a slippery Cassie and a slippery Wenzel state, respectively. (a,b) are reprinted with permission from (Anand et al., 2012), Copyright 2012 American Chemical Society. (c,d) are reproduced with permission from (Dong et al., 2018), (e,f) are reproduced with permission from (Dai et al., 2015).

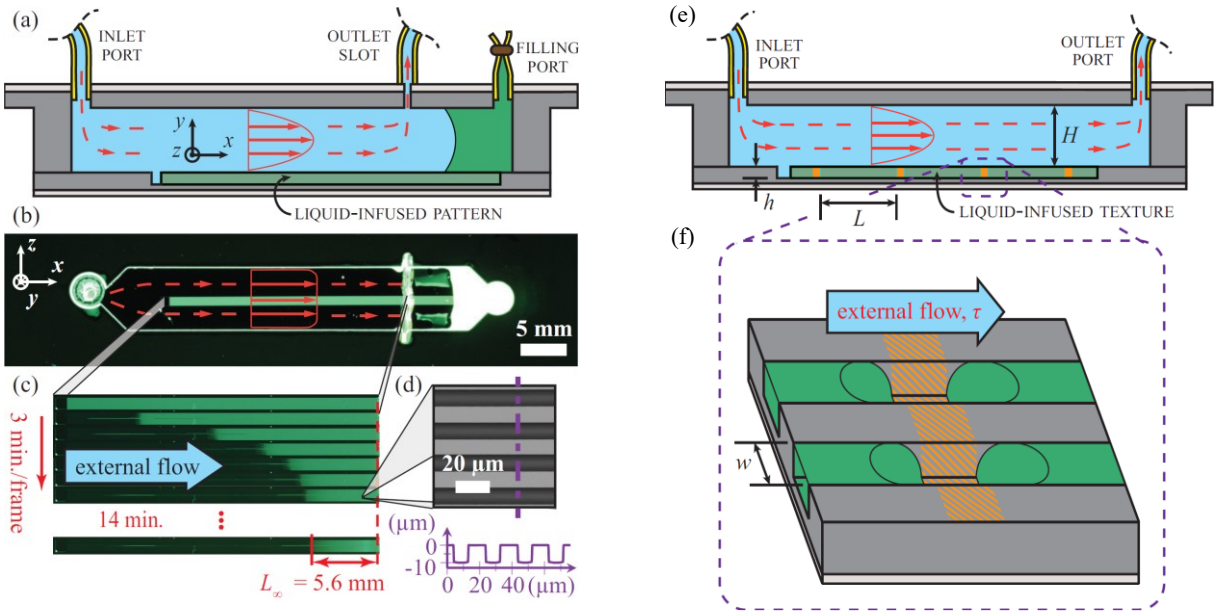

Figure 3: Shear driven failure of LIS with parallel grooves together with a solution that prevents drainage of the grooves. (a) Schematic of a flow cell with liquid-infused grooves at the bottom. (b) Top view in which the green fluorescence of the grooves becomes visible. (c) Time-lapse images showing the drainage of the grooves until a steady-state filling length L_∞ is reached. (d) Structure of the grooves in top view and in a schematic cross section. (e) Schematic of a flow cell with liquid-infused grooves and hydrophilic stripes (orange) orthogonal to the grooves. (f) Schematic showing a section of the bottom wall, indicating the distribution of lubricant inside the grooves. Panels a, b, c and d are reprinted with permission from (Wexler at al. 2015a), Copyright 2015 by the American Physical Society; panels e and f are reprinted with permission from (Wexler at al. 2015b), Copyright 2015 American Chemical Society.

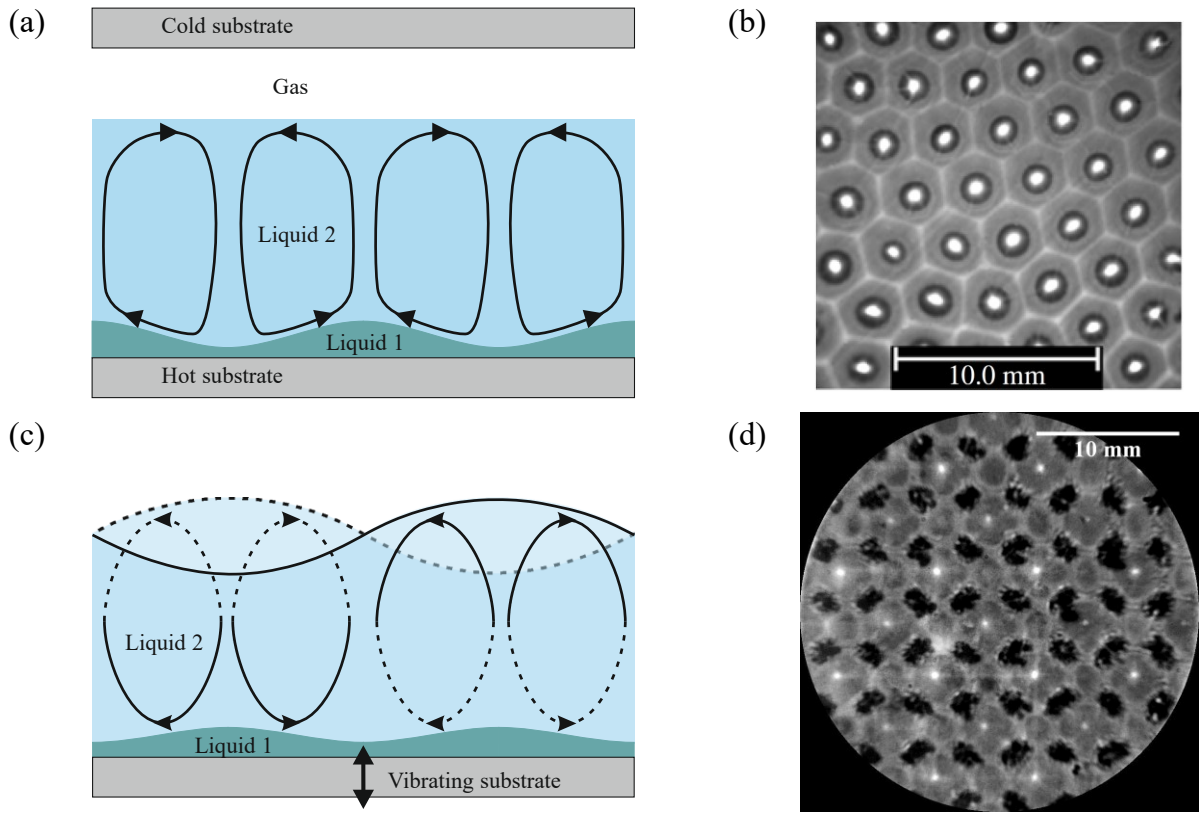

Figure 4: Sculpting of lubrication films by self-organized cellular flow patterns. (a) Schematic of the Bénard-Marangoni instability on a lubrication film. The closed lines indicate the streamlines of the flow. (b) Hexagonal array of flow cells as observed in the experiments. Reproduced with permission from (Nejati et al. 2015). (c) Schematic of the Faraday instability on a lubrication film. The closed lines indicate the streamlines of the flow at two different points in time separated by half the oscillation period of the Faraday waves. The full (dashed) streamlines correspond to the surface deformation indicated by the full (dashed) line. (d) Square array of flow cells as observed in the experiments. Reproduced with permission from (Zhao et al. 2019).

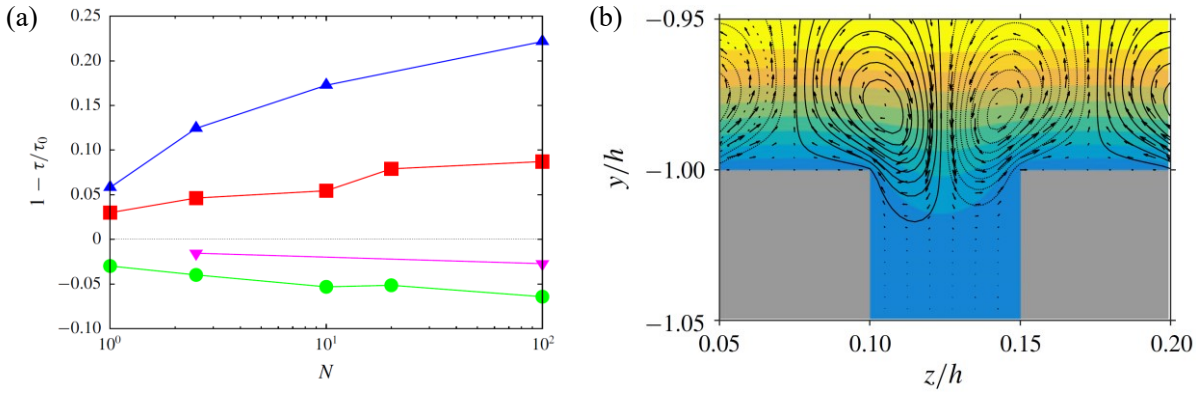

Figure 5: (a) Drag reduction of different LIS in turbulent flow as a function of viscosity ratio. ■ longitudinal grooves ($a = 0.5$), ● transverse grooves ($a = 0.5$), ▼ staggered cubes ($a = 0.5$), ▲ staggered cubes ($a = 0.875$). a denotes the liquid-liquid area fraction. (b) Streamlines of the time-averaged secondary flow field over a surface indentation for longitudinal grooves. The colormap represents the time-averaged streamwise velocity. Reproduced with permission from (Arenas et al. 2019).

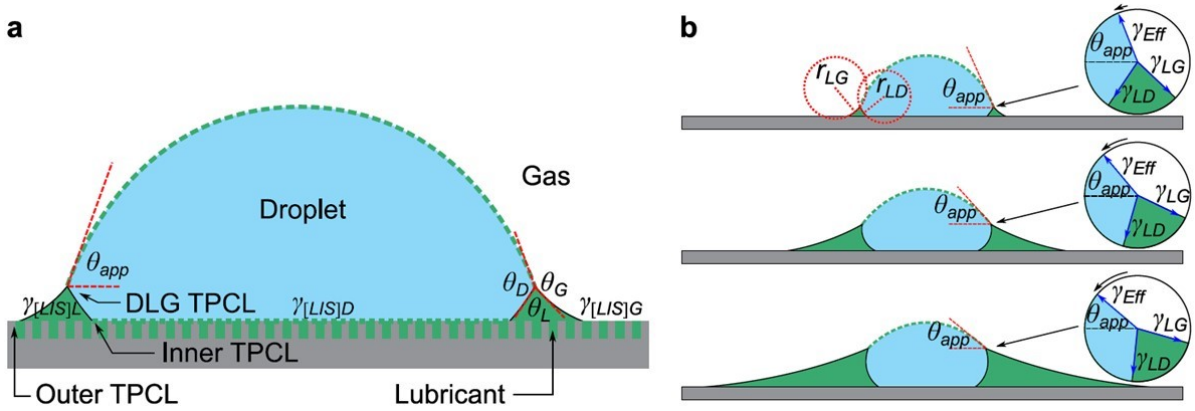

Figure 6: A drop on a LIS. (*a*) The apparent contact angle defined at the drop/lubricant/gas three-phase contact line and associated Neumann angles. The dashed drop outline shows possible cloaking by the lubricant (i.e. infused liquid). The three–phase contact lines (DLG TPCL, Inner TPL and Outer TPCL) do not exist if the lubricant cloaks the drop or wets the solid surface structure in the presence of the drop or gas, respectively. (*b*) The wetting ridge height and rotation of the Neumann triangle increase with lubricant film pressure relative to the drop, thus reducing the apparent contact angle. Adapted from Semprebon *et al*. (2017) [**Note to Annual Reviews: McHale is an author of this article; the publisher grants authors the right to reuse their own figures without permission.**]

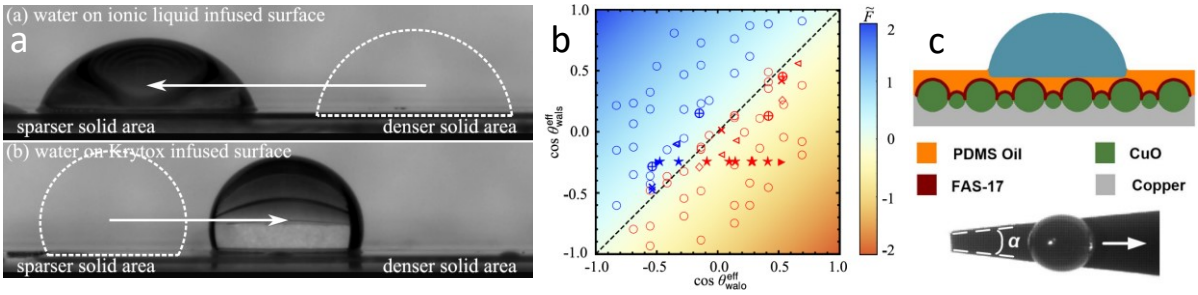

Figure 7: Drop motion driven by wetting. (*a*) lubricant determined bidirectional driving forces on topographical solid gradient LIS and (*b*) simulation and experimental data for sign dependence of wetting forces (Sadullah, *et al.*, 2020) [**Note to Annual Reviews: McHale is an author of this article; the publisher grants authors the right to reuse their own figures without permission.**]. (*c*) Motion on shape gradient LIS (Reproduced with permission from Zheng et *al.*, 2017; Copyright (2017) by the American Chemical Society).

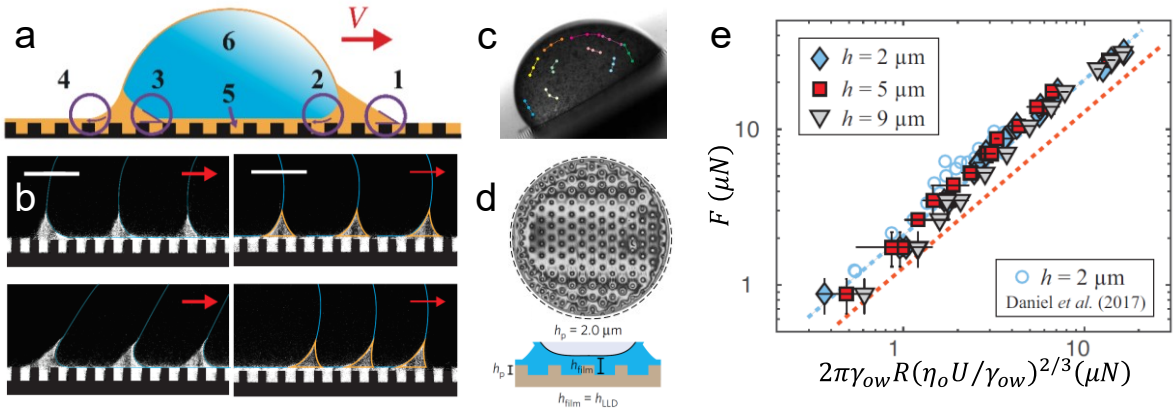

Figure 8: Drop friction. (*a*) Six dynamical regions for a drop moving on a LIS and (*b*) images of the rear and front foot of moving drops at low and high velocities (Adapted with permission from Keiser et al., 2020; Copyright (2020) by the American Physical Society. Additional image reproduced with permission from Keiser (2018) with data provided by P. Baumli and A. Kaltbeitzel). (*c*) Trajectories of particles relative to a water drop revealing drop rolling (Reproduced with permission from Smith *et al.*, 2013; Copyright (2013) by the Royal Society of Chemistry). (*d*) White-light interferometry of the film below an oleoplaning drop (Adapted by permission from Nature Publishing Group: Daniel et al., 2017; Copyright (2017)). (*e*) Landau-Levich induced transition between two regimes of friction, both obeying a 2/3 power law, at large capillary number (Keiser et al., 2020 as adapted with permission from Keiser, 2018; Copyright (2020) by the American Physical Society).

References

Anand S, Paxson AT, Dhiman R, Smith JD, Varanasi KK. 2012. Enhanced condensation on lubricant-impregnated nanotextured surfaces. *ACS Nano* 6:10122-10129

Andreotti B, Snoeijer JH, 2020. Statics and dynamics of soft wetting. *Annu. Rev. Fluid Mech.* 52:285–308

Arenas I, García E, Fu MK, Orlandi P, Hultmark M, Leonardi, S. 2019. Comparison between super-hydrophobic, liquid infused and rough surfaces: a direct numerical simulation study. *J. Fluid Mech.* 869:500-525

Barrio-Zhang H, Ruiz-Gutiérrez É, Armstrong S, McHale G, Wells GG, Ledesma-Aguilar R. 2020. Contact-angle hysteresis and contact-line friction on slippery liquid-like surfaces. *Langmuir* 36:15094–15101

Barthlott W, Neinhuis C. 1997. Purity of the sacred lotus, or escape from contamination in biological surfaces. *Planta* 202:1-8.

Bico J, Reyssat É, Roman B. 2018. Elastocapillarity: When surface tension deforms elastic solids. *Annu. Rev. Fluid Mech.* 50:629–659

Bico J, Tordeux C, Quere D. 2001. Rough wetting. *Europhys. Lett.* 55:214-220.

Bohn HF, Federle W. 2004. Insect aquaplaning: Nepenthes pitcher plants capture prey with the peristome, a fully wettable water-lubricated anisotropic surface. *P. Natl. Acad. Sci. USA* 101: 14138-14143

Boreyko JB, Chen CH. 2009. Self-propelled dropwise condensate on superhydrophobic surfaces. *Phys. Rev. Lett.* 103:184501

Bormashenko E. 2010. Wetting transitions on biomimetic surfaces. *Phil. Trans. R. Soc. A*:368, 4695-4711

Brabcova Z, McHale G, Wells GG, Brown CV, Newton MI. 2017. Electric field induced reversible spreading of droplets into films on lubricant impregnated surfaces. *Appl. Phys. Lett.* 110:121603

Busse A, Sandham ND, McHale G, Newton MI. 2013. Change in drag, apparent slip and optimum air layer thickness for laminar flow over an idealised superhydrophobic surface. *J. Fluid Mech.* 727:488-508

Chang J, Jung T, Choi H, Kim J. 2019. Predictions of the effective slip length and drag reduction with a lubricated micro-groove surface in a turbulent channel flow. *J. Fluid Mech.* 874:797-820

Chen X, Wen G, Guo Z. 2020. What are the design principles, from the choice of lubricants and structures to the preparation method, for a stable slippery lubricant-infused porous surface? *Mater. Horiz.* 7: 1697-1726

Chen H, Zhang P, Zhang L, Liu H, Jiang Y, Zhang D, Han Z, Jiang L. 2016. Continuous directional water transport on the peristome surface of Nepenthes alata. *Nature* 532:85-89

Dai X, Stogin BB, Yang S, Wong TS. 2015. Slippery Wenzel state. *ACS Nano* 9:9260-9267

Daniel D, Timonen JVI, Li R, Velling SJ, Kreder MJ, Tetreault A, Aizenberg J. 2018. Origins of extreme liquid repellency on structured, flat, and lubricated hydrophobic surfaces. *Phys. Rev. Lett.* 120:244503.

Daniel D, Timonen JVI, Li R, Velling SJ, Aizenberg J. 2017. Oleoplaning droplets on lubricated surfaces. *Nat. Phys.* 13:1020–1025

Davis SH. 1987. Thermocapillary instabilities, *Annu. Rev. Fluid Mech.* 19:403-435

Dong Z, Schumann MF, Hokkanen MJ, Chang B, Welle A, Zhou Q, Ras RHAA, Xu Z, Wegener M, Levkin PA. 2018. Superoleophobic slippery lubricant-infused surfaces: combining two extremes in the same surface. *Adv. Mater.* 30:1803890

Eifert A, Paulssen D, Varanakkottu SN, Baier T, Hardt S. 2014. Simple fabrication of robust water-repellent surfaces with low contact-angle hysteresis based on impregnation. *Adv. Mater. Interfaces* 1:1–5

Epstein AK, Wong TS, Belisle R, Boggs EM, Aizenberg J. 2012. Liquid-infused structured surfaces with exceptional anti-biofouling performance. *Proc. Natl. Acad. Sci.* 109:13182-13187

Fu MK, Arenas I, Leonardi S, Hultmark M. 2017. Liquid-infused surfaces as a passive method of turbulent drag reduction. *J. Fluid Mech.* 824:688-700

Furmidge CGL. 1962. Studies at phase interfaces. 1. Sliding of liquid drops on solid surfaces and a theory for spray retention. *J. Colloid Sci.* 17:309–324

Gao L, McCarthy TJ. 2008. Teflon is hydrophilic. Comments on definitions of hydrophobic, shear versus tensile hydrophobicity, and wettability characterization. *Langmuir* 24:9183–9188

Gao N, Geyer F, Pilat DW, Wooh S, Vollmer D, Butt HJ, Berger R. 2018. How drops start sliding over solid surfaces. *Nat. Phys.* 14:191–196

Ge Z, Holmgren H, Kronbichler M, Brandt L, Kreiss G. 2018. Effective slip over partially filled microcavities and its possible failure. *Phys. Rev. Fluids* 3:054201

Golovin KB, Gose JW, Perlin M, Ceccio SL, Tuteja A. 2016. Bioinspired surfaces for turbulent drag reduction. *Phil. Trans. R. Soc. A* 374: 20160189

Guan JH, Ruiz-Gutiérrez É, Xu B, Wood D, McHale G, Ledesma-Aguilar R, Wells G. 2017. Drop transport and positioning on lubricant-impregnated surfaces. *Soft Matter* 13:3404-3410.

Guan JH, Wells GG, Xu B, McHale G, Wood D, Martin J, Stuart-Cole S. 2015. Evaporation of sessile droplets on slippery liquid-infused porous surfaces (SLIPS). *Langmuir* 31:11781–11789

Hao C, Liu Y, Chen X, He Y, Li Q, Li KY, Wang Z. 2014. Electrowetting on liquid-infused

film (EWOLF): Complete reversibility and controlled droplet oscillation suppression for fast optical imaging. *Sci. Rep.* 4:1–7

Hocking, LM. 1976. A moving fluid interface on a rough surface. *J. Fluid Mech.* 76:801-817

Howell C, Grinthal A, Sunny S, Aizenberg M, Aizenberg J. 2018. Designing liquid-infused surfaces for medical applications: a review. *Adv. Mater.* 30:1-26

Huang C, Guo Z. 2019. Fabrications and applications of slippery liquid-infused porous surfaces inspired from nature: a review. *J. Bionic Eng.* 16:769-793

Jacobi I, Wexler JS, Stone HA. 2015. Overflow cascades in liquid-infused substrates. *Phys. Fluids* 27:082101

Karpitschka S, Das S, van Gorcum M, Perrin H, Andreotti B, Snoeijer JH. 2015. Droplets move over viscoelastic substrates by surfing a ridge. *Nat. Commun.* 6:7891

Karpitschka S, Pandey A, Lubbers LA, Weijs JH, Botto L, Das S, Andreotti B, Snoeijer JH. 2016. Liquid drops attract or repel by the inverted Cheerios effect. *Proc. Natl. Acad. Sci.* 113:7403–7407

Keiser A. 2018. Dynamiques sur des surfaces texturées et imprégnées. PhD Thesis. Sorbonne Université, Français. NNT : 2018SORUS601

Keiser A, Baumli P, Vollmer D, Quéré D. 2020. Universality of friction laws on liquid-infused materials. *Phys. Rev. Fluids* 5:014005

Keiser A, Keiser L, Clanet C, Quéré D. 2017. Drop friction on liquid-infused materials. *Soft Matter* 13:6981-6987

Kim P, Kreder MJ, Alvarenga J, Aizenberg J. 2013. Hierarchical or not? Effect of the length scale and hierarchy of the surface roughness on omniphobicity of lubricant-infused substrates. *Nano Lett.* 13:1793-1799

Kreder MJ, Alvarenga J, Kim P, Aizenberg J. 2016. Design of anti-icing surfaces: smooth, textured or slippery? *Nat. Rev. Mater.* 1:15003

Kreder MJ, Daniel D, Tetreault A, Cao Z, Lemaire B, Timonen JVI, Aizenberg J. 2018. Film dynamics and lubricant depletion by droplets moving on lubricated surfaces. *Phys. Rev. X* 8:31053

Kusumaatmaja H, McHale G, Semprebon C, Sadullah MS. 2021. A note on LIS ridge rotation. arXiv.

Lafuma, A, Quéré D. 2003. Superhydrophobic states. *Nat. Mater.* 2:457–460

Lafuma A, Quéré D. 2011. Slippery pre-suffused surfaces. *Europhys. Lett.* 96:56001

Latthe SS, Sutar RS, Bhosale AK, Nagappan S, Ha CS, Sadasivuni KK, Liu S, Xing R. 2019. Recent developments in air-trapped superhydrophobic and liquid-infused slippery surfaces for anti-icing application. *Prog. Org. Coatings* 137:105373

Launay G, Sadullah MS, McHale G, Ledesma-Aguilar R, Kusumaatmaja H, Wells GG. 2020. Self-propelled droplet transport on shaped-liquid surfaces. *Sci. Rep.* 10:14987

Lei W, Rigozzi MK, McKenzie DR. 2016. The physics of confined flow and its application to water leaks, water permeation and water nanoflows: a review. *Rep. Prog. Phys.* 79:025901

Leonardi S, Castro, IP. 2010. Channel flow over large cube roughness: a direct numerical simulation study. *J. Fluid Mech.* 651:519–539

Liu Y, Wexler JS, Schönecker C, Stone HA. 2016. Effect of viscosity ratio on the shear-driven failure of liquid-infused surfaces. *Phys. Rev. Fluids* 1:074003

Lou X, Huang Y, Yang X, Zhu H, Heng L, Xia F. 2020. External stimuli responsive liquid-infused surfaces switching between slippery and nonslippery states: fabrications and applications. *Adv. Funct. Mater.* 30:1-21

Luo JT, Geraldi NR, Guan JH, McHale G, Wells GG, Fu Y. 2017. Slippery liquid-infused porous surfaces and droplet transportation by surface acoustic waves. *Phys. Rev. Appl.* 7:014017.

Manukyan G, Oh JM, van den Ende D, Lammertink RGH, Mugele F. 2011. Electrical switching of wetting states on superhydrophobic surfaces: A route towards reversible Cassie-to-Wenzel transitions. *Phys. Rev. Lett.* 106:014501

McCarthy J, Vella D, Castrejón-Pita AA. 2019. Dynamics of droplets on cones: Self-propulsion due to curvature gradients. *Soft Matter* 15:9997–10004

McHale G, Orme BV, Wells GG, Ledesma-Aguilar R. 2019. Apparent contact angles on lubricant-impregnated surfaces/SLIPS: From superhydrophobicity to electrowetting. *Langmuir* 35:4197–4204

Miles J, Henderson D. 1990. Parametrically forced surface waves. *Annu. Rev. Fluid Mech.* 22:143-165

Nejati I, Dietzel M, Hardt S. 2015. Conjugated liquid layers driven by the short-wavelength Bénard–Marangoni instability: experiment and numerical simulation, *J. Fluid Mech.* 783: 46-71

Nizkaya TV, Asmolov ES, Vinogradova OI. 2014. Gas cushion model and hydrodynamic boundary conditions for superhydrophobic textures. *Phys. Rev. E* 90:043017

Papadopoulos P, Mammen L, Deng X, Vollmer D, Butt HJ. 2013. How superhydrophobicity breaks down. *P. Natl. Acad. Sci. USA* 110:3254-3258

Park KC, Kim P, Grinthal A, He N, Fox D, Weaver JC, Aizenberg J. 2016. Condensation on slippery asymmetric bumps. *Nature* 531:78-82

Paulssen D, Feng W, Pini I, Levkin PA, 2018. Formation of liquid-liquid micropatterns through guided liquid displacement on liquid-infused surfaces. *Adv. Mater. Interfaces* 5: 1800852.

Paulssen D, Hardt S, Levkin PA. 2019. Droplet sorting and manipulation on patterned two-phase slippery lubricant-infused surface, *ACS Appl. Mater. Interfaces* 11:16130-16138.

Peppou-Chapman S, Hong JK, Waterhouse A, Neto C. 2020. Life and death of liquid-infused surfaces: a review on the choice, analysis and fate of the infused liquid layer. *Chem. Soc. Rev.* 49:3688-3715

Quéré, D. 2005. Non-sticking drops. *Rep. Prog. Phys.* 68:2495–2532

Quéré, D. 2008. Wetting and roughness. *Annu. Rev. Mater. Res.* 38:71–99

Rofman B, Dehe S, Frumkin V, Hardt S, Bercovici M. 2020. Intermediate states of wetting on hierarchical superhydrophobic surfaces. *Langmuir* 36:5517-5523

Rosenberg BJ, Van Buren T, Fu MK, Smits AJ. 2016. Turbulent drag reduction over air- and liquid- impregnated surfaces. *Phys. Fluids* 28:015103

Rothstein JP. 2010. Slip on superhydrophobic surfaces, *Annu. Rev. Fluid Mech.* 42:89-109

Ruiz-Gutiérrez É, Guan JH, Xu B, McHale G, Wells GG, Ledesma-Aguilar R. 2017. Energy invariance in capillary systems. *Phys. Rev. Lett.* 118:218003

Sadullah MS, Launay G, Parle J, Ledesma-Aguilar R, Gizaw Y, McHale G, Wells GG, Kusumaatmaja H. 2020a. Bidirectional motion of droplets on gradient liquid infused surfaces. *Commun. Phys.* 3:166

Sadullah MS, Panter JR, Kusumaatmaja H. 2020b. Factors controlling the pinning force of liquid droplets on liquid infused surfaces. *Soft Matter* 16:8114–8121

Sadullah MS, Semprebon C, Kusumaatmaja H. 2018. Drop dynamics on liquid-infused

surfaces: The role of the lubricant ridge. *Langmuir* 34:8112–8118

Scarratt RJ, Zhu L, Neto C. 2020. Large effective slip on lubricated surfaces measured with colloidal probe AFM. *Langmuir* 36:6033-6040

Schatz MF, Neitzel GP. 2001, Experiments on thermocapillary instabilities. *Annu. Rev. Fluid Mech.* 33:93-127

Schellenberger F, Xie J, Encinas N, Hardy A, Klapper M, Papadopoulos P, Butt HJ, Vollmer D. 2015. Direct observation of drops on slippery lubricant-infused surfaces. *Soft Matter* 11, 7617–7626

Schönecker C, Baier T, Hardt S. 2014. Influence of the enclosed fluid on the flow over a microstructured surface in the Cassie state. *J. Fluid Mech.* 740:168-195

Seiwert J, Clanet C, Quéré D. 2011. Coating of a textured solid. *J. Fluid Mech.* 669:55–63

Semprebon C, McHale G, Kusumaatmaja H. 2017. Apparent contact angle and contact angle hysteresis on liquid infused surfaces. *Soft Matter* 13:101–110

Semprebon C, Sadullah MS, McHale G, Kusumaatmaja H. 2021. Apparent contact angle of droplets on liquid infused surfaces: geometric interpretation. Soft Matter. In press (Advance article: https://pubs.rsc.org/en/Content/ArticleLanding/2021/SM/D1SM00704A). See also arXiv preprint arXiv:2105.04805.

Sharma M, Roy PK, Barman J, Khare K. 2019. Mobility of aqueous and binary mixture drops on lubricating fluid-coated slippery surfaces. Langmuir 35:7672–7679

Shirtcliffe NJ, McHale G, Atherton S, Newton MI. 2010. An introduction to superhydrophobicity. *Adv. Colloid Interface Sci.* 161:124–138

Smith JD, Dhiman R, Anand S, Reza-Garduno E, Cohen RE, McKinley GH, Varanasi KK. 2013. Droplet mobility on lubricant-impregnated surfaces. *Soft Matter* 9:1772–1780

Solomon BR, Khalil KS, Varanasi KK. 2014. Drag reduction using lubricant-impregnated surfaces in viscous laminar flow. *Langmuir* 30:10970-10976

Solomon BR, Subramanyam SB, Farnham TA, Khalil KS, Anand S, Varanasi KK. 2017. Lubricant-impregnated surfaces in *Non-wettable Surfaces: Theory, Preparation, and Applications* (edited by Ras RHA, Marmur A): 285-318, The Royal Society of Chemistry

Tao R, McHale G, Reboud J, Cooper JM, Torun H, Luo JT, Luo J, Yang X, Zhou J, Canyelles-Pericas P, Wu Q, Fu Y. 2020. Hierarchical nanotexturing enables acoustofluidics on slippery yet sticky, flexible surfaces. *Nano Lett.* 20:3263–3270

Tress M, Karpitschka S, Papadopoulos P, Snoeijer JH, Vollmer D, Butt HJ. 2017. Shape of a sessile drop on a flat surface covered with a liquid film. *Soft Matter* 13:3760–3767

Van Buren T, Smits AJ. 2017. Substantial drag reduction in turbulent flow using liquid-infused surfaces. *J. Fluid Mech.* 827:448-456.

Villegas M, Zhang Y, Abu Jarad N, Soleymani L, Didar TF. 2019. Liquid-infused surfaces: a review of theory, design, and applications. *ACS Nano* 13:8517-8536

Wells GG, Ruiz-Gutiérrez É, Le Lirzin Y, Nourry A, Orme BV, Pradas M, Ledesma-Aguilar R. 2018. Snap evaporation of droplets on smooth topographies. *Nat. Commun.* 9:1380

Wexler JS, Grosskopf A, Chow M, Fan Y, Jacobi I, Stone HA. 2015b. Robust liquid-infused surfaces through patterned wettability. *Soft Matter* 11:5023-5029

Wexler JS, Jacobi I, Stone HA. 2015a. Shear-driven failure of liquid-infused surfaces, *Phys. Rev. Lett.* 114:168301

Wong TS, Kang SH, Tang SKY, Smythe EJ, Hatton BD, Grinthal A, Aizenberg J. 2011. Bioinspired self-repairing slippery surfaces with pressure-stable omniphobicity. *Nature* 477:443-447

Xiao R, Li JS, Mieszkin S, Di Fino A, Clare AS, Callow ME, Callow JA, Grunze M,

Rosenhahn A, Levkin PA. 2013a. Slippery liquid-infused porous surfaces showing marine antibiofouling properties, *ACS Appl. Mater. Interfaces* 5:10074-10080

Ybert C, Barentin C, Cottin-Bizonne C, Joseph P, Bocquet L. 2007. Achieving large slip with superhydrophobic surfaces: Scaling laws for generic geometries. *Phys. Fluids* 19:123601

Zhang C, Zhang B, Ma H, Li Z, Xiao X, Zhang Y, Cui X, Yu C, Cao M, Jiang L. 2018. Bioinspired pressure-tolerant asymmetric slippery surface for continuous self-transport of gas bubbles in aqueous environment. *ACS Nano* 12:2048–2055

Zhao S, Dietzel M, Hardt S. 2019. Faraday instability of a liquid layer on a lubrication film. *J. Fluid Mech.* 879: 422-447

Zheng Y, Cheng J, Zhou C, Xing H, Wen X, Pi P, Xu S. 2017. Droplet motion on a shape gradient surface. *Langmuir* 33:4172–4177